Robotica (2010) volume 28, pp. 279–296. © Cambridge University Press 2009
doi:10.1017/S026357470999035X

Toward an optimal performance index for neurosurgical robot's design

Alessandro Gasparetto and Vanni Zanotto*

DIEGM, Università degli Studi di Udine, via delle Scienze 208, Udine 33100, Italy

(Received in Final Form: July 23, 2009. First published online: September 2, 2009)

SUMMARY

In the past years a large number of new surgical devices have been developed to improve the operation outcomes and reduce the patient's trauma. Nevertheless, the dexterity and accuracy required in positioning the surgical tools are often unreachable if the surgeons are not assisted by a suitable system. Since a medical robot works in an operating room, close to the patient and the medical staff, it has to satisfy much stricter requirements with respect to an industrial one. From a kinematic point of view, the robot must reach any target position in the patient's body, being as less invasive as possible for the surgeon's workspace. In order to meet such requirements, the right robot structure has to be chosen by means of the definition of suitable kinematic performance indices.

In this paper some task-based indices based on the robot workspace and stiffness are presented and discussed. The indices will be used in a multiobjective optimization problem to evaluate best robot kinematic structure for a given neurosurgical task.

KEYWORDS: Medical robotics; Robot design; Robot performances; Neurosurgery; Kinematics, Task-based index.

1. Introduction

Robotic systems were applied to surgery in the early 1980s.[1] Initial experimentations with surgical robotics largely consisted in adapting to this field the already-existing industrial-robot technologies. If for industrial robotics, repeatability, flexibility, and speed are usually the most important concerns, surgical robots put instead patients' safety above everything else.

In the last decade, within the medical community there has been a growing awareness of the benefits offered by using robots in various medical tasks.[1] These benefits include cost reduction, precision improvement, and even less pain to the patient. Admittedly, robots can perform accurate and repeatable tasks which would be impossible to be replicated by any surgeon. Clearly, the potential interaction between robotic systems and surgeons is producing a new worldwide interest in the area of medical robotics. Medical robotics has found a fruitful ground in neurosurgical applications, owing to the accuracy in tool positioning[2] required by the high functional density of the central nervous system. Modern neurosurgery has reached a point at which the scale of the operative field is so small that even skilled surgeons are reaching the limits of their dexterity.[3,4] Moreover novel treatments, such as intracellular inclusion of genomic subcellular implants used in transgenic technology, require an accuracy of 10 μm. Currently, this technology is limited to animal models, but if transposed to the operating room on human subjects, such precision would be reachable only through robotic assistance. This is due to the following: (i) the brain is firmly held in a solid container, allowing fixation of devices to hold it in position during procedures; (ii) the anatomical topology is fairly stable, corresponding to a rather well-known functional somatotopy; (iii) brain imaging has been the most progressing field during the past decades, combining several modalities; (iv) the brain is the organ in which the highest precision is required for surgical procedures; (v) stereotactic procedures have opened the way to numerical approaches through minimally invasive routes.

Key neurosurgical applications include stereotactic neurosurgery, robotized microscopes, endoscopic neurosurgery, tumor resection, and telepresence.

CT-guided stereotactic brain surgery[5] was one of first robotic-assisted applications in surgery. Stereotactic surgery is a branch of neurosurgery that involves the use of a precision apparatus to guide the surgical tool accurately into the brain, so as to reach a deep target in safe conditions, with no direct monitoring of the surgical site.[6] Basically the frame-based system allows the coordinate system of the frame to stay with the patient's head. The typical stereotactic frame-based registration used in many hospitals is a base ring which is positioned and secured to the skull using four screws. Thus CT and MRI image slices can be accurately referred to the frame in three dimensions. This has been used for many years for stereotactic biopsies in which the extraction needle can be positioned with good accuracy and reliability. In modern frameless systems the coordinate system of the patient's head is registered just before or during surgery. In order to reduce patient's trauma, a frameless stereotactic system positioned over the surgical area can be considered the best solution for a stereotactic robotic system. However the frameless accuracy for the robotic positioning should be within the tolerance dictated by the surgical operation.

The first documented application of medical robotics in neurosurgery was in 1985 when Know *et al.*[7] used the commercial robot PUMA 200 by Unimation as positioning device for a biopsy instrument. In 1991 Drake[8] used the same robot as retraction device in the surgical management

* Corresponding author. E-mail: vanni.zanotto@uniud.it

of thalamic astrocytomas. Despite their novel application, both systems lacked the proper safety features needed for widespread acceptance into neurosurgery. In the beginning of 1987, Benabid *et al.*[9] experimented with an early precursor to the robot marketed as NeuroMate (Integrated Surgical Systems, Sacramento, CA). NeuroMate uses preoperative image data for assisting with surgical planning and a passive robotic arm to perform the procedure.[10]

NeuroMate is a five-axis open-chain robot. It can be used both in frame-based and in frameless neurosurgical operations. In frame-based operations, the patient's head is held by means of a mechanical frame which works as precise reference for the tool positioning. In frameless operations, on the other hand, there are no mechanical structures on the patient's head, but some special markers allow a vision system to estimate the correct head position. Up until now, the accuracy of NeuroMate in the frameless configuration is not less than 2 mm (owing to the precision of the vision system),[11] while in the frame-based configuration the positioning accuracy is better than 0.5 mm.

Neurobot[12,13] is a manipulator made of two robots: the first one is a gantry robot which works as gross-motion positioner for the second one, a four-axis robot which moves the surgical tool during the operations. The decoupling of the two-robot motion increases the safety of the operation, since it reduces the mechanical components moving close to the patient. Moreover, since the number of actuators is reduced, the system features a higher level of accuracy. Neurobot is employed principally as an actuator for neurosurgical endoscopes.

Evolution 1 is another example of robotized endoscope.[14] It is made of a five-axis robot which moves a parallel robot, on which a linear actuator moving the surgical tools is fixed. The first robot acts as gross-motion positioner, while the last allows a fine movement.

Liu *et al.*[15] have presented a master–slave robotic system, named NeuroMaster, developed at the Robotics Institute of Beihang University, P. R. China. NeuroMaster is a five-axis serial robot. The first axis is a prismatic joint, while the four remaining joints are revolute. The prismatic joint allows a high accuracy in the vertical positioning of the tool.

An up-to-date overview of the most significant researches performed in this field can be found in ref. [1] and in the references reported therein.

Many robot design variables such as structure (serial vs. parallel), geometry, actuators (rotary vs. prismatic), and reduction ratios are important to design a novel robot. Unfortunately, any change that enhances one performance attribute will almost always detract from another.

There is a close relationship between the kinematic performance and design of robot manipulators. Because of this, in the past decades, several robot design criteria have been proposed for the kinematic evaluation and for designing a well-conditioned robot manipulator that has a dexterous workspace. The main objective of these studies was to develop a dexterity measuring system (manipulator singularity-avoidance capabilities) by establishing a performance index.

Given the close relationship between kinematic design and manipulator workspace, many authors have studied the workspace and singularity analysis of robot manipulators, performed a numerical approach to determining if the workspace was formulated, and solved by tracing boundary surfaces of a workspace, as in ref. [16]. Some authors developed performance indices that could be used as an optimization and design criteria and defined the determinant of the Jacobian as the manipulability of a robot manipulator and proposed it as a performance criterion. Another performance index commonly used is the condition number of the Jacobian matrix as reported in ref. [16]. It is possible to define another global performance index as reported in ref. [17], directly based on the condition number.

Other approaches are based on the measure of isotropy, for example, in ref. [18]. In ref. [19] four new performance indices for control of 6R robots are presented. Two of them depend on the end-effector and are based on the operation ellipsoid and on an object-oriented metric in the workspace respectively. Two other indices are independent of the end-effector and reflect the distance of the actual posture from the closest singularity. All these indices are characterized by an invariance under similarities, have a geometric meaning, and are computable in real time, so they can be used for the control of manipulator in real time. About this argument, other significant works can also be found in refs. [20–24].

2. Neurosurgical Robot Design Based on Task Specifications

A universally optimum medical robot does not exist, but optimality only exists in the context of a specific application, since different applications have different performance demands.

This paper describes how a robot can be designed for a particular neurosurgical application.

In surgical robot design two goals have to be reached first, the maximum robot workspace and the highest accuracy in tool positioning. The first goal requires the preliminary remarks to know the neurosurgical task to allow an optimum criterion for choosing the suitable kinematic structure of the robot. The second goal concerns the mechanical properties of robot links and transmissions. Unfortunately, this usually contradicts the workspace design goal. Therefore a suitable optimization has to be defined to meet both the two goals.

Additional constraints arise when the robot works in the frame-based configuration, since the stereotactic frame restricts the robot workspace. As a result some robot configurations belonging to the dexterous workspace become unreachable, since the links collide against the stereotactic frame. Therefore, in designing a new neurosurgical robot the operative task has to be defined previously, making clear both the operative space (tool positions and orientations) and the position of the spatial constraints.

During a neurosurgical operation the patients lie on the surgical bed and lean on their back or rest on one side. The stereotactic frame is fixed to the patient's head. During a manual procedure the stereotactic frame works as an accurate tool-holder. In a robotized neurosurgical procedure, on the other hand, it works as reference frame which allows the matching between the CT images and the current head position. Typical surgical tools are biopsy cannula, drills,

https://doi.org/10.1017/S026357470999035X Published online by Cambridge University Press

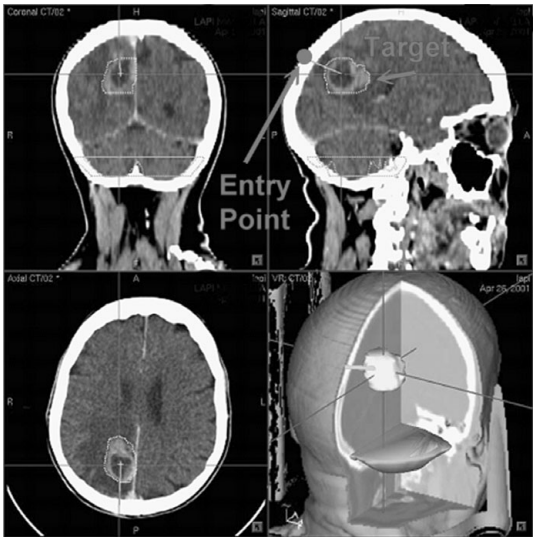

Fig. 1. EP and target.

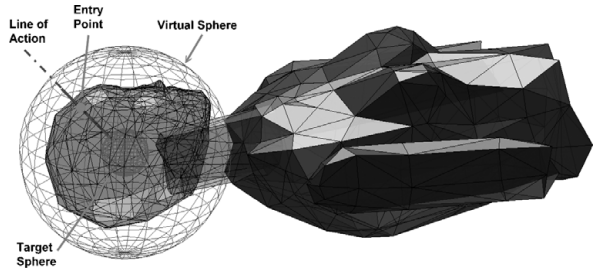

Fig. 2. Virtual sphere centered on patient's head.

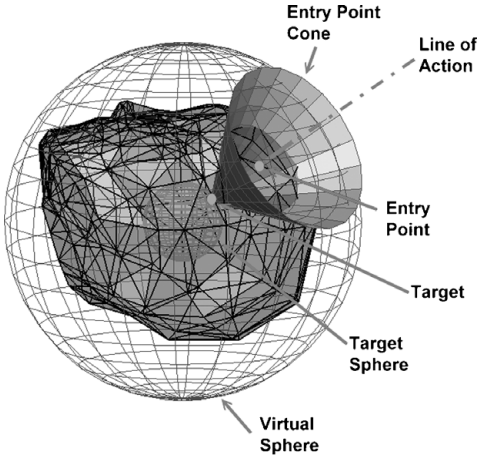

Fig. 3. Virtual sphere, TS, and EPC.

electrodes, and probes. All the mentioned tools have axial symmetry (around the main axis), thus have fixed only five spatial constraints, the position, and the orientation of the main axis of the tool. Moreover only two spatial points on the patient's head have to be stated by the surgeons. The first one is the target point (TP), the center of the cerebral lesion in which the tool has to be placed, while the second one is the entry point (EP), the hole through which the surgical instruments go into the skull (Fig. 1). The EP and TP define the line of action (LoA) along which the tool should be moved (Figs. 1 and 2). The TP can be localized in any region belonging to the cerebral tissue. The EP, on the other hand, has to be chosen carefully by the surgeon. The choice depends both on the target position and on the linear trajectory that will be followed by the surgical tool. The trajectory shall avoid passing through any vital part. Hence both the deepness of the surgical operation and the orientation of the surgical tool depend on the position of the EP. The motion of the surgical tool through the brain tissue follows a linear trajectory in order to limit the trauma on the tissues. During a robotized surgical operation making use of a usual neurosurgical robot, such as NeuroMate, the surgical tool movements into the skull are performed manually by the surgeon. On the robot end-effector a suitable tool-holder is fixed. Once the tool-holder has been moved close to the patient's head and has been oriented along the desired direction, the robot is switched off. Therefore, the operation continues manually, following the direction fixed by the tool-holder. Usually the end-effector trajectory is planned so that the tool-tip position coincides with the target when the extreme location of the tool along the tool-holder has been reached.

Owing to safety reasons, no interpolated trajectories are allowed into the cerebral tissues, since these depend on the concurrent actions of several actuators; thus the risk for the patient is too high. Therefore, such a procedure is named *passive*, since the robot does not work actively during the surgical operation.

In the *active* robotic procedure, on the other hand, a linear actuator on the end-effector allows the precise and controlled movement of the surgical tool along the desired LoA. Therefore the robot is able to work during the surgical operation too. However, for safety reasons, the robot shall stay always away from the patient's head, beyond a suitable distance. It is useful to define a suitable *region of safety* (Fig. 2), close to the patient's head. Owing to the spatial form of the head the shape of this region can be chosen spherical. The safety region defines the area that shall be inaccessible by the robot, and then it shall comprise the stereotactic frame as well. The *safety sphere* is only a virtual entity; thus in the following it will be referred to as *virtual sphere*. The robot shall be able to move the surgical tool in the desired configuration, keeping its links far from the virtual sphere.

It is useful to define a further virtual sphere, named *target sphere* (TS), which depends on the mean length of the standard surgical tools. The TS is concentric with the virtual sphere, but its radius is smaller (Fig. 2). The TS defines the region of the deepest TP and then fixes the robot's *worst case* working configuration. Clearly the TS depends on the surgical-tool dimensions. The tip of the surgical tool shall reach every point on the TS surface, and the tool shall be oriented along any desired direction. The set of the required tool orientations on the generic point of the TS surface is bounded, since the distance between the EP and the target shall be kept limited for the surgical reasons that have been stated above. Therefore a suitable cone, named EP cone (EPC) (Fig. 3), can be defined for every point **P** on the TS surface. The vertex of EPC coincides with point **P**, and its axis is oriented along the line perpendicular to the TS surface in **P**. Consequently, the set of the overall tool orientations on the generic point can be defined by means of the EPC.

https://doi.org/10.1017/S026357470999035X Published online by Cambridge University Press

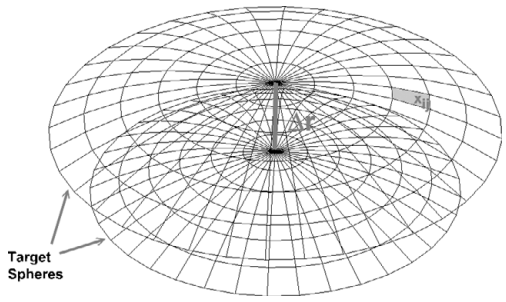

Fig. 4. TS surface grid.

Once the neurosurgical task has been defined, the requirements of the working space can be accurately taken, as will be discussed in the next section.

3. Task-Based Workspace Evaluation

The workspace is one of the main goals for the kinematic design of surgical manipulators.

The workspace evaluation in this work follows the approach defined in ref. [20]. The mapping for the forward kinematics of a manipulator with n degrees of freedom (DOFs), or an n-DOF manipulator, with r-dimensional task space can be expressed in the form

$$\mathbf{F}_K : \mathbf{R}^n \rightarrow \mathbf{R}^r \,|\, \mathbf{p} = \mathbf{F}_K(\mathbf{q}). \tag{1}$$

The task space represents all task-allowed positions and orientations of the manipulator end-effector. A general numerical evaluation of the task space can be obtained by formulating a suitable binary representation of the surface of the TS. Once the inverse kinematic problem (IKP) has been solved, it is possible to map each point (thought as an r-dimensional vector comprising both the position and the orientation of the surgical tool) belonging the robot workspace to the corresponding set of points in the joints space. Therefore, a binary matrix $\mathbf{W}$ can be defined on the TS surface as follows.

For each grid pixel $\mathbf{x}_{ij}$ (Fig. 4) belonging to the surface of the TS, all the (discrete) directions $\mathbf{d}_{kl}$ belonging to the EPC cone $\Lambda(\mathbf{x}_{ij})$ are considered.

If the IKP admits, at least, one configuration such that all the links are external to the virtual sphere, the corresponding matrix element $\mathbf{w}_{\mathbf{X},ij} = \mathbf{W}_{\mathbf{X}}(i, j)$ is set to one; otherwise the element is set to zero.

The generic point $\mathbf{x}_{ij}$ on the surface of the TS is defined as shown in Fig. 4:

$$\mathbf{x}_{ij} = \mathbf{C} + \begin{Bmatrix} r_T \sin\theta_i \cos\varphi_j \\ r_T \sin\theta_i \sin\varphi_j \\ r_T \cos\theta_i \end{Bmatrix}, \quad \theta_i \in [0, \pi], \varphi_j \in [-\pi, \pi], \tag{2}$$

where $\mathbf{C}$ is the center of the virtual sphere; r_T is the TS radius; $(r_T, \theta_i, \varphi_j)$ are the spherical coordinates of the generic point on the TS surface; and

$$i = \left[\frac{\theta + \Delta\theta}{\Delta\theta}\right], \quad j = \left[\frac{\varphi + \Delta\varphi}{\Delta\varphi}\right] \tag{3}$$

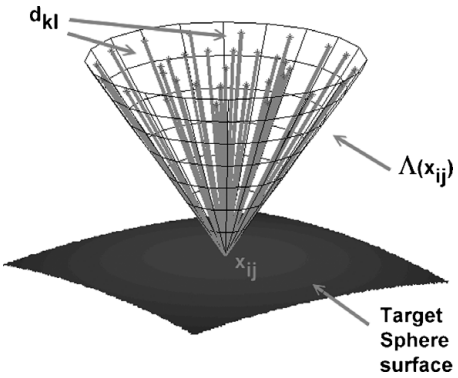

Fig. 5. The required directions on the generic point of the TS surface.

in which $\Delta\theta$ and $\Delta\varphi$ are the resolution parameters of the grid mesh for the scanning process.

In a similar way, the generic direction belonging to the cone $\Lambda(\mathbf{x}_{ij})$ (Fig. 5) can be defined, in the local reference frame, as

$$\mathbf{d}_{kl} = \begin{Bmatrix} \sin\gamma_k \cos\beta_l \\ \sin\gamma_k \sin\beta_l \\ \cos\gamma_k \end{Bmatrix}, \quad \gamma_k \in [-\alpha, \alpha], \beta_l \in [-\pi, \pi], \tag{4}$$

where α is the characteristic angle of the TP cone, and

$$k = \left[\frac{\gamma + \Delta\gamma}{\Delta\gamma}\right], \quad l = \left[\frac{\beta + \Delta\beta}{\Delta\beta}\right], \tag{5}$$

where $\Delta\gamma$ and $\Delta\beta$ are the resolution parameters of the grid mesh for scanning the directions belonging to the target cone.

The proposed binary representation is useful for a numerical evaluation of the robot workspace area, referred to the chosen TS:

$$A_T = \sum_{i=1}^{i_{\max}} \sum_{j=1}^{j_{\max}} w_{ij} r_T^2 \sin\theta_i \Delta\theta \Delta\varphi. \tag{6}$$

Therefore the first performance index can be defined as

$$I_A = \frac{A_T}{4\pi r_T^2} \tag{7}$$

which describes the capabilities of the robot to reach every point $\mathbf{x}$ on the TS surface along any direction belonging to the associated EPC cone.

The workspace volume can be computed by spanning the TSs and considering the sum of the corresponding workspace areas:

$$V = \sum_{r_T,\min}^{r_T,\max} A_T \Delta r, \tag{8}$$

where Δr is the resolution for the TS radius. Therefore the second performance index is

$$I_V = \frac{3V}{4p\left(r_{T,\max}^3 - r_{T,\min}^3\right)}, \tag{9}$$

https://doi.org/10.1017/S026357470999035X Published online by Cambridge University Press

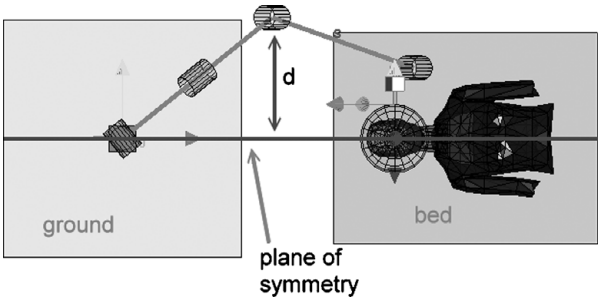

Fig. 6. Robot invasiveness.

where $r_{T,\min}$ and $r_{T,\max}$ are the minimum and maximum radii of the considered TSs respectively.

A further index to evaluate the robot performances can be obtained if the function $\mathbf{w}_{ij}$ is modified in such a way that the average number $\mathbf{s}_{ij}$ of solutions for each $\mathbf{d}_{kl} \in \Lambda(\mathbf{x}_{ij})$ is returned from the inverse kinematic algorithm.

Therefore a new matrix $\mathbf{S}_T = [\mathbf{s}_{ij}]$ can be defined for each TS. This matrix allows the surgeon to know the number of allowable configurations for each target and choose, therefore, the suitable EP.

4. Robot Invasiveness Evaluation

In the robot design process particular attention must be given in the robot *invasiveness* evaluation. The word refers, in this work, to the portion of the surgeon workspace used by the robot during the surgical task. Actually the invasiveness is one of the obstacles which limit the use of medical robots.

Therefore, the goal is to reduce the robot invasiveness in such a way that the surgeon and the medical staff are able to move near the patient as though the robot were not in the surgical room.

The invasiveness depends on the link arrangement, which, on the other hand, depends on the current robot configuration. Therefore a suitable index of invasiveness can be defined as

$$I_I = \max_{(\mathbf{P}_t, \mathbf{z}_t)} \left[\min_{C_j} \left(\max_{i=1,\ldots,n} \{d_i\} \right) \right], \tag{10}$$

where d_i is the distance between the origin of the reference frame of the ith link and the plane of symmetry of the surgical bed (Fig. 6) and $\mathbf{z}_t$ is the desired tool direction .

If the robot admits more than one configuration (C_j) for the same tool position, the index considers the one that is less invasive.

Finally the index evaluation considers each couple point-direction $(\mathbf{P}_t, \mathbf{z}_t)$ belonging to the task-based workspace defined in Section 3.

The invasiveness due to the trajectory followed by the robot to reach the target configuration can be neglected, since it takes much less time with respect to the surgical task.

Therefore the index evaluation can be done only on the final robot configuration.

5. Stiffness Evaluation

When a manipulator performs a given task, the end-effector exerts some forces and/or moments on its environment. This contact force will cause the end-effector to be deflected away from its desired location. Intuitively, the amount of deflection is a function of the applied force and stiffness of the manipulator. Thus the stiffness of a manipulator has a direct impact on the position accuracy. The overall stiffness of a manipulator depends on several factors, including the size of and the material used for the links, the mechanical transmission mechanism, the actuators, and the controller.

Several approaches to define the stiffness properties of a manipulator have been proposed in the literature.[25,26]

In this work a simplified stiffness matrix, making use of lumped parameters and superposition principle, will be considered, in accordance with the approach presented in ref. [20] and the assumptions taken therein.

The stiffness properties of a manipulator can be defined through the "Cartesian stiffness matrix" $\mathbf{K}$. This matrix gives the relation between the vector of the compliant displacements $\Delta\mathbf{S}$ occurring at the end-effector when a static wrench $\mathbf{W}$ acts upon it:

$$\mathbf{W} = \mathbf{K}\Delta\mathbf{S}. \tag{11}$$

The stiffness matrix can be computed by defining a suitable model of the manipulator, which takes into account lumped stiffness parameters of links and motors. The stiffness models with lumped parameters proposed in ref. [20] can take into account the compliance of both actuators and links along and about x, y, and z directions. They are based on the assumption of small compliant displacements. Under this assumption the superposition principle holds. Thus, the compliance of each link and actuator can be considered as an additive term to the overall compliance. Moreover, the effects of tension/compression, bending, and torsion stiffness of a link can be considered as additive terms to the stiffness of the link itself. These additive terms can be defined as lumped parameters, and they can be represented as linear or torsion springs. A tensional spring will represent effects of torsion and bending. Therefore, the stiffness matrix of a generic beam element can be written as reported for example in ref. [26].

A 6×6 stiffness matrix $\mathbf{K}$ of a manipulator can be derived through the composition of suitable matrices. A first matrix $\mathbf{C}_F$ gives the relationship between the vector of all the wrenches acting on each link when a wrench $\mathbf{W}$ acts on the manipulator extremity according to the expression

$$\mathbf{W} = \mathbf{C}_F\mathbf{W}_L. \tag{12}$$

The matrix $\mathbf{C}_F \in \mathbf{R}^{6\times N}$ represents the force transmission capability of the manipulator mechanism, with N being the number of links of the manipulator. Therefore, for a six-DOF PUMA-like robot, $\mathbf{C}_F = \mathbf{J}^{-T}$, where $\mathbf{J}$ is the manipulator Jacobean matrix.

Also, $\mathbf{W}_L \in \mathbf{R}^N$ can be written in a simplified form, as the vector of motor torques when the only source of compliance is assumed to be given by motors. The second matrix $\mathbf{K}_P \in \mathbf{R}^{N\times N}$ gives the possibility to compute the vector $\Delta\mathbf{v}$ of all the deformations of the links when each wrench $\mathbf{W}_{Li}$ on the ith link given by $\mathbf{W}_L$ acts on the legs according to

$$\mathbf{W}_L = \mathbf{K}_P\Delta\mathbf{v}. \tag{13}$$

https://doi.org/10.1017/S026357470999035X Published online by Cambridge University Press

The matrix $\mathbf{K}_P$ groups the values of the lumped stiffness parameters for the deformable components of a manipulator structure. The vector $\Delta\mathbf{v}$ comprises the joint angular displacements when the only source of compliance is assumed to be given by motors. A third matrix $\mathbf{C}_K$ gives the vector $\Delta\mathbf{S}$ of compliant displacements at the end-effector due to the displacements of the manipulator links:

$$\Delta\mathbf{v} = \mathbf{C}_K \Delta\mathbf{S}. \tag{14}$$

The matrix $\mathbf{C}_K \in \mathbf{R}^{N\times 6}$ expresses the kinematics of a manipulator. Therefore, the stiffness matrix $\mathbf{K}$ can be computed as

$$\mathbf{K} = \mathbf{C}_F \mathbf{K}_P \mathbf{C}_K. \tag{15}$$

The stiffness matrix $\mathbf{K}$ can be used to compute the accuracy performance. In fact, the vector of compliant displacements $\Delta\mathbf{S}$ can be evaluated by using Eq. (11) once the matrix $\mathbf{K}$ is determined and static wrench acting on the movable platform is given.

From the above-mentioned considerations four indices that take into account stiffness performance can be defined:

$$\sqrt{\Delta S_x^2 + \Delta S_y^2 + \Delta S_z^2} = \Delta_{\text{pos}}, |\Delta S_\varphi|, |\Delta S_\psi|, |\Delta S_\theta|, \tag{16}$$

where Δ_{pos} is the compliant linear displacement and ΔS_φ, ΔS_ψ, ΔS_θ are the errors on tool orientation.

6. Optimization Problem

The indices defined in Sections 3–5 can be used to describe an optimization problem able to maximize the performances for the given robot kinematic structure and the desired surgical task, by choosing the suitable links length $(\ell_1, \ldots, \ell_k)$.

The optimization problem can be expressed as follows:

$$\begin{aligned} p = &\max_{\ell_1,\ldots,\ell_k} \left(I_A(\bar{r}_T) + \frac{\xi}{I_I} + I_V \right) \\ &\text{s. t.} \\ &\text{(a) } \Delta_{\text{pos}} < \Delta_{\text{pos,max}}, \\ &\text{(b) } \Delta S_\varphi, \Delta S_\psi, \Delta S_\theta < \Delta_{or,\text{max}}, \\ &\text{(c) } \ell_j \in L_j = [\ell_{j,\text{min}}, \ell_{j,\text{max}}], \text{ and} \\ &\text{(d) } r_T \in [r_{T,\text{min}}, r_{T,\text{max}}]. \end{aligned} \tag{17}$$

The cost function considers the workspace area index I_A computed in the nominal TS $(\bar{r}_T)$, while the volume index I_V and the invasiveness index I_I are evaluated on the nominal target volume defined by $[r_{T,\text{min}}, r_{T,\text{max}}]$.

The factor ξ has been introduced to make homogeneous the terms of the cost function.

Constraints (a) and (b) concern the robot accuracy stated in Section 5.

7. Robot Design Procedure

The design procedure described below can be followed to choose the suitable robot structure and the right link dimensions:

1. Define the robot accuracy by specifying the upper limits $\Delta_{\text{pos,max}}$ and $\Delta_{\text{or,max}}$.
2. Choose a trial robot kinematic structure.
3. Solve the optimization problem of the previous section.
4. Repeat steps 2 and 3 for different robot structures.
5. Compare the p indices obtained and choose the suitable robot structure.

8. Numerical Example

The design procedure and the indices defined in the previous sections will be implemented in the next to found the optimal robot structure for a particular neurosurgical task. The task makes use of a robotic tool-holder which moves a miniaturized X-ray source named Photon Radiosurgery System (PRS, by Carl Zeiss).[27] The aim is to design the robotic arm able to move the tool-holder in such a way that the probe of the X-ray source can reach each point in the cerebral tissue, according to what has been defined in Section 3.

8.1. Neurosurgery by means of PRS and two special tool-holders

The Mechatronics Research Group (composed of researchers of the University of Padova, the University of Udine, and the University of Trieste, all in Italy) with the assistance of the Neurosurgical Department of the University of Florence (Italy) has developed two master–slave robotic systems for minimally invasive neurosurgical operations.

The first robot, named Linear Actuator for NeuroSurgery (LANS[28]) has been conceived specifically to perform biopsies and neurosurgical interventions by means of PRS, whose emitting tip must be placed accurately inside the patient's brain tissues.[27] The LANS robotic system is composed of a haptic master module, operated by the surgeon, and a slave mechatronic module (Fig. 7) moving the PRS probe, or a biopsy needle, along a predefined emission axis in accordance with the master position imposed by the surgeon. In order to orient the LANS along the established emission axis, a robotic arm is needed. The currently used arm is a commercial NeuroMate robot, employed in a frame-based configuration which ensures the highest possible accuracy. The system has been designed assuming that during the surgical operation, only the LANS (which is very accurate and provides the surgeon with force feedback) is in active mode while NeuroMate is powered off. This allows overcoming much of the problems associated with the complex nature of this surgical therapy. Moreover, very precise and repeatable movements of the biopsy needle and of the X-ray source can be obtained, thus improving the overall intervention outcomes.

Double Action Actuator for NeuroSurgery (DAANS[29]) is the second robot (Figs. 8 and 9) built by the Mechatronics research group. The aim of the system is to provide another DOF to the PRS source about the emission axis. The system allows extending the therapy with PRS also to

https://doi.org/10.1017/S026357470999035X Published online by Cambridge University Press

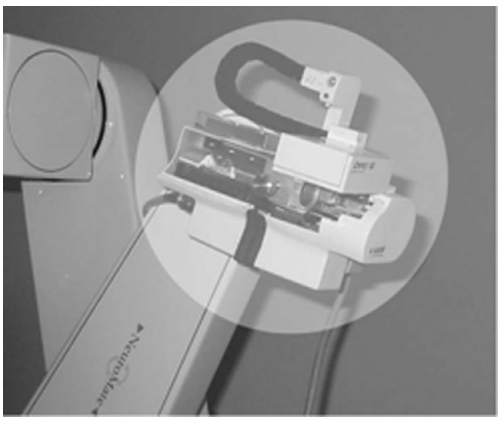

Fig. 7. LANS actuator fixed on the NeuroMate arm.

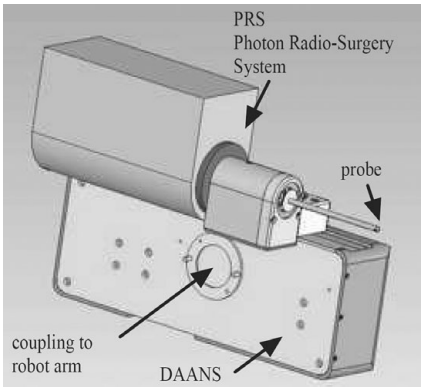

Fig. 8. DAANS actuator.

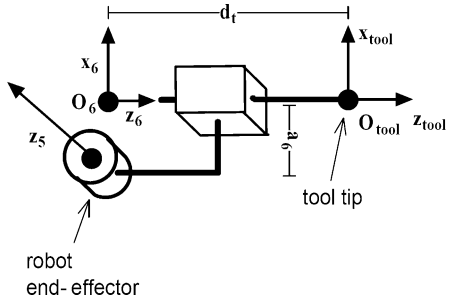

Fig. 9. DAANS schematic.

irregular-shape tumorous lesions, by integrating translation and spin movements of the source. Nevertheless, LANS and DAANS limit the NeuroMate mobility, owing to their geometrical dimension, which can interfere with the robot arm movements. In this manner the NeuroMate workspace is reduced and some tool configurations are not reachable.

In the next sections, first the proposed indices will be used to evaluate the performances of the actual robotic system; then they will be employed to choose the optimal robot kinematic structure to perform the surgical task by PRS and DAANS. Owing to the constraints on the robot invasiveness, only serial kinematic structures will be considered. For the same reason, spherical manipulators have been not contemplated, even though the shape of the surgical task could suggest the use of this kind of robot. Moreover, the mechanical stiffness of a spherical manipulator is low, and the wrist positioning accuracy decreases as the radial stroke

Table I. DAANS Denavit–Hartenber parameters.

${}^{i-1}T_i$	σ_i	a_i(mm)	α_i (rad)	d_i (mm)	θ_i (rad)
${}^{base}P_0$	1	0	$\frac{\pi}{2}$	942	$\frac{\pi}{2}$
${}^{0}P_1$	0	125	0	0	q_1

Table II. Virtual sphere and TSs parameters.

Parameter	Value
α	30°
$R_{\text{virtual sphere}}$	250 mm
r_T	$100 \div 130$ mm
$\bar{r}_T$	130 mm
C	$[1034\,\text{mm},\ 0,\ 942\,\text{mm}]^T$

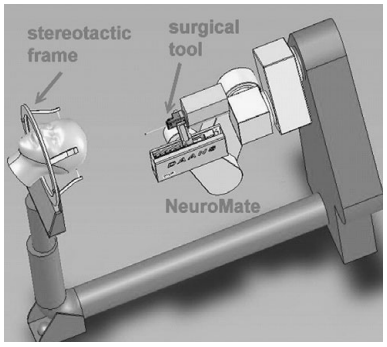

Fig. 10. NeuroMate, DAANS, and PRS.

increases. These considerations become a strong limit for the use of spherical manipulator in the mentioned neurosurgical task and suggest the use of a different kinematic structure, as will be presented in next sections.

The Denavit–Hartenberg parameters of the DAANS are described in Table I, while the dimensions and the characteristics of the virtual spheres and the TSs are defined in Table II.

8.2. Surgical task by means of NeuroMate

NeuroMate is a five-link commercial robot (shown in Fig. 10) specifically conceived to perform neurosurgical interventions. As a matter of fact, the number of DOFs matches exactly the dimension of a usual neurosurgical task (Section 3). The aim of this section is to evaluate the NeuroMate performance when it performs the surgical task as has been defined in the previous section, which requires the use of DAANS and PRS (Fig. 10). The Denavit–Hartenberg parameters of the robot are described in Table III(a) (where the "standard Denavit–Hartenberg notation" has been used; σ_i describes the kinematic of the current joint: $\sigma_i = 1$ stands for a prismatic joint, while $\sigma_i = 0$ stands for a revolute joint). The accuracy properties of the NeuroMate can be found in ref. [11], and they will be not discussed in this work. The IKP, on the other hand, will be solved in the Appendix, since nowadays, no literature exists for the NeuroMate IKP.

Once the IKP has been solved, it is possible to estimate the workspace performance indices following the definition given in Section 3. In particular, considering the matrix $\mathbf{W_X}$

https://doi.org/10.1017/S026357470999035X Published online by Cambridge University Press

Table III. (a) NeuroMate Denavit–Hartenber parameters.

${}^{i-1}T_i$	σ_i	a_i[mm]	α_i (rad)	d_i (mm)	θ_i (rad)
${}^{base}P_0$	1	0	$\frac{\pi}{2}$	942	$\frac{\pi}{2}$
${}^{0}P_1$	0	${a_1}^a$	0	0	q_1
${}^{1}P_2$	0	0	$-\frac{\pi}{2}$	${d_2}^a$	q_2
${}^{2}P_3$	0	${a_3}^a$	0	0	q_3
${}^{3}P_4$	0	${a_4}^a$	0	0	q_4
${}^{4}P_5$	0	85	$\frac{\pi}{2}$	0	q_5
${}^{5}P_{\text{tool tip}}$	1	0	0	138	0

[a]The numerical values have been omitted, since they are property of Integrated Surgical Systems Inc. (ISS).

for the given TS (Table II) and introducing the suitable surface S_W, described through the points

$$S_W(i, j) = (1 + w_{ij}) \begin{bmatrix} \sin\theta_i \cos\varphi_j \\ \sin\theta_i \sin\varphi_j \\ \cos\theta_i \end{bmatrix},$$
$$\theta_i \in [0, \pi], \quad \varphi_j \in [-\pi, \pi], \tag{18}$$

it is possible to have a graphical representation of the robot workspace (Fig. 11). It can be shown that only a subregion of the target surface (corresponding to the parietal and occipital regions of the skull) can be reached by the overall robotic system (NeuroMate and DAANS).

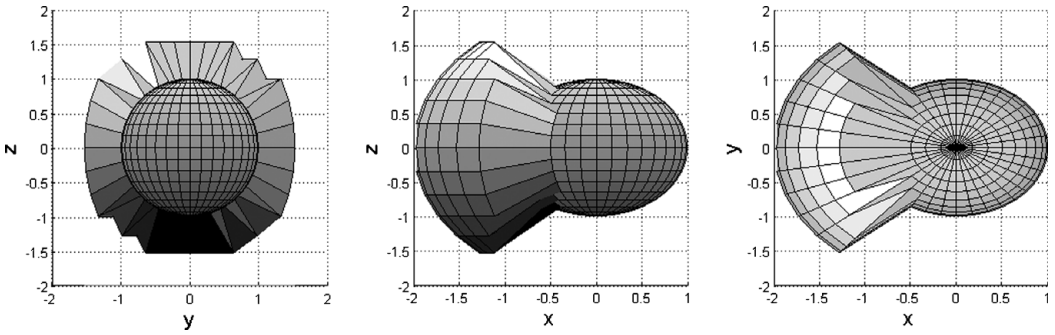

Fig. 11. NeuroMate S_W surface.

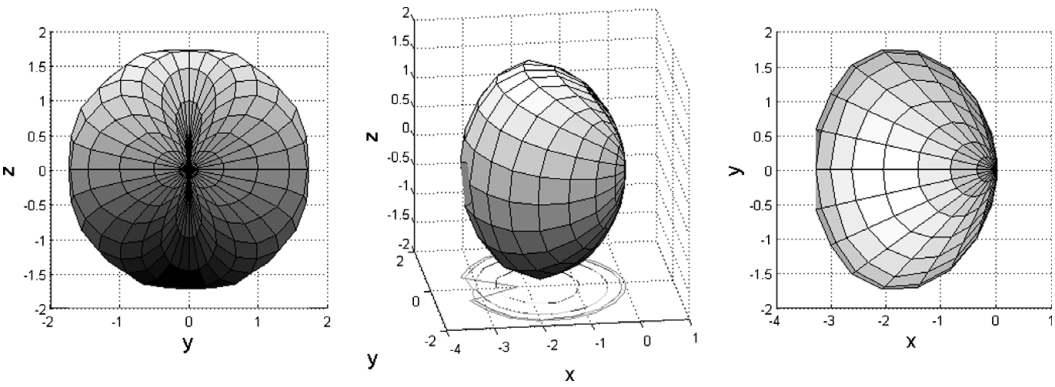

Fig. 12. NeuroMate S_S surface.

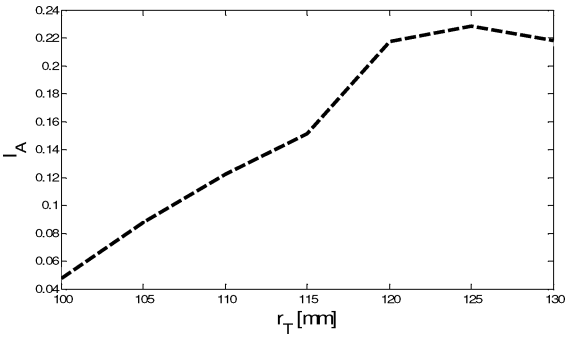

Fig. 13. Index I_A in function of the TS radius.

In a similar manner, it is possible to define the surface S_S corresponding to the matrix $\mathbf{S}_T$ of Section 3:

$$S_S(i, j) = s_{ij} \begin{bmatrix} \sin\theta_i \cos\varphi_j \\ \sin\theta_i \sin\varphi_j \\ \cos\theta_i \end{bmatrix}, \theta_i \in [0, \pi], \ \varphi_j \in [-\pi, \pi]. \tag{19}$$

From surface S_S it is possible to highlight the robot capabilities: the best performances can be obtained on the occipital region, on which the robot admits, on average, three different solutions for the same tool configuration (Fig. 12).

Figure 13 shows the performance index I_A as a function of the TS radius. It can be observed that the index decreases when the radius drops to lower values, and it remains always well under the unit.

https://doi.org/10.1017/S026357470999035X Published online by Cambridge University Press

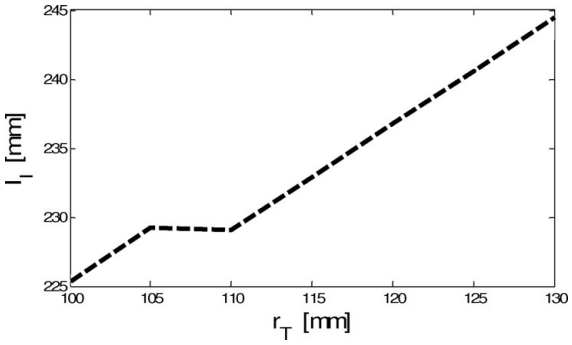

Fig. 14. Index I_I in function of the TS radius.

The index I_V for NeuroMate is $I_V = 0.19$. Therefore only one fifth of the considered target volume (Table II) can be reached by the robot.

The invasiveness index I_I is shown in Fig. 14. Its value varies linearly with the TS radius, since it depends principally on the same critical tool configuration, which corresponds to the parietal region of the skull.

It must be recalled that these values have been computed only on the reachable configurations, which are a subset of the required robot configurations. Therefore the comparison with those that will be obtained in the next sections is misleading.

From the above analysis appears that NeuroMate has been conceived to work only on a particular region of the patient's head, which corresponds to occipital and parietal zones. Moreover the invasiveness index is up to 250 mm, which means that the surgeon's workspace is still preserved in spite of the robot presence.

8.3. Toward an optimal robotic arm design

In this section the procedure described in Section 7 will be followed to optimize the design of a new robotic arm able to overcome the limits on the target workspace pointed out in the previous paragraph for the NeuroMate arm. The procedure starts with the design optimization of two different well-known robots: the anthropomorphic arm and the Stanford manipulator. Then the results will be compared with those obtained with a special robot, named Neurobud, whose particular kinematic structure has been conceived at the University of Udine.

All the robots feature six DoFs, resulting to be redundant with respect to the task space dimension (Section 3). The redundancy is a very useful property for surgical robots, since the additional DoF can be properly used to improve the invasiveness performances, as has been discussed in ref. [30]. Nevertheless the choice of the additional DoF must be done with care, since it may imply accuracy errors due the reduced robot stiffness.

8.3.1. Anthropomorphic manipulator. The first robot under optimization is a usual six-DoF anthropomorphic manipulator, (Fig. 15) whose Denavit–Hartenberg parameters are shown on Table III(b). The IKP can be solved as in ref. [31].

The optimization problem works on the second and third links, since the robot workspace depends mainly on their lengths (a_2 and d_4). No constraints have been taken on joint mobility to avoid additional requirements on the optimization problem. A suitable simplified stiffness model for this manipulator can be found in ref. [20]. The matrix $\mathbf{K}_P$ defined in Section 3 becomes a diagonal matrix whose elements are assumed be equal to $k_{T1} = k_{T2} = k_{T3} = 4.67 \times 10^8$ Nm and $k_{T4} = k_{T5} = k_{T6} = 4.67 \times 10^6$ Nm, according to what has been discussed in ref. [20].

Table III. (b) Anthropomorphic arm Denavit–Hartenber parameters.

i	${}^{i-1}T_i$	σ_i	a_i (mm)	α_i (rad)	d_i (mm)	θ_i (rad)
0	${}^{base}P_0$	1	0	0	272	0
1	${}^{0}P_1$	1	0	0	670	0
2	${}^{1}P_2$	0	0	$\frac{\pi}{2}$	0	q_1
3	${}^{2}P_3$	0	a_2	0	0	q_2
4	${}^{3}P_4$	0	0	$-\frac{\pi}{2}$	0	q_3
5	${}^{4}P_5$	0	0	$\frac{\pi}{2}$	d_4	q_4
6	${}^{5}P_6$	0	0	$-\frac{\pi}{2}$	0	q_5
7	${}^{6}P_7$	0	0	0	0	q_6
8	${}^{7}P_8$	1	0	$\frac{\pi}{2}$	85	$\frac{\pi}{2}$
	${}^{8}P_{\text{tool tip}}$	1	0	0	138	0

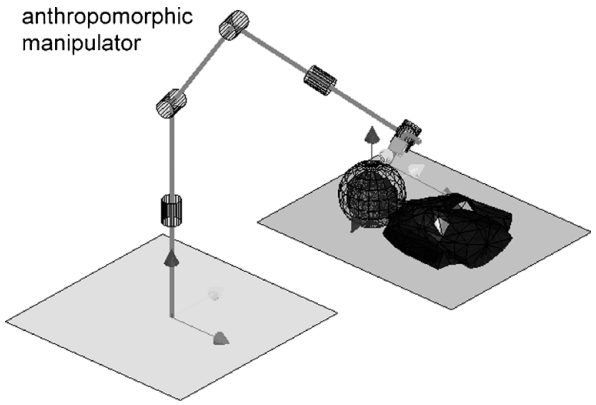

Fig. 15. Anthropomorphic arm.

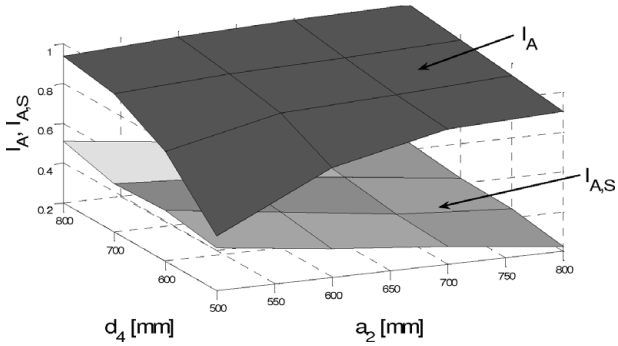

Fig. 16. Functions of I_A and $I_{A,S}$ for the anthropomorphic arm.

Figure 16 shows the workspace index I_A versus link lengths. The TS (defined in Table II) is completely reachable ($I_A = 1$) only for the link length on the bounds of the considered intervals ($a_2 = d_4 = 800$ mm).

Nevertheless, assuming the accuracy constraints on the optimization problem, as specified in Table III, the reachability drops drastically, as can be shown by the function $I_{A,S}$ in Fig. 16. The function $I_{A,S}$ considers the index I_A filtered by the effects of robot stiffness which limits accuracy. The maximum, $I_{A,S} = 0.51$, is achieved for $a_2 = 500$ mm and $d_4 = 800$ mm.

https://doi.org/10.1017/S026357470999035X Published online by Cambridge University Press

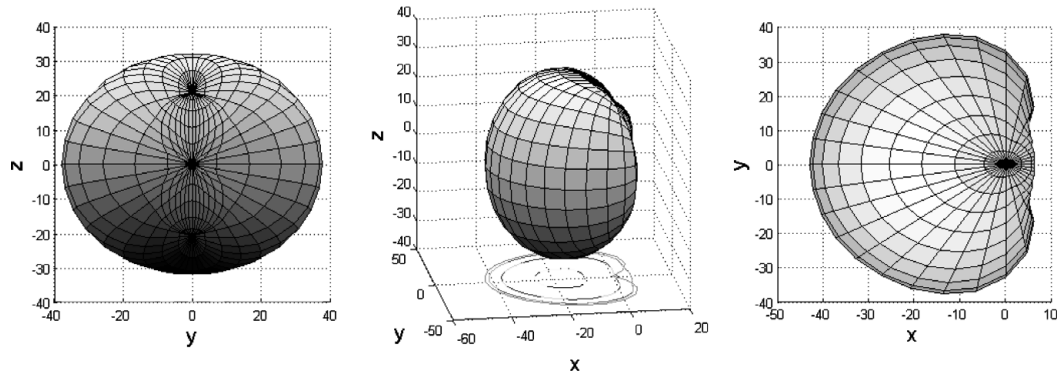

Fig. 17. Anthropomorphic arm S_S surface.

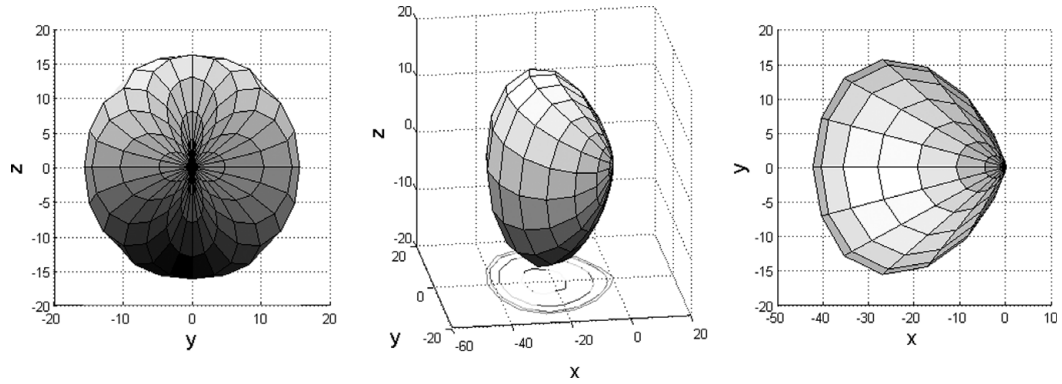

Fig. 18. Anthropomorphic arm S_S surface filtered by the accuracy constraints.

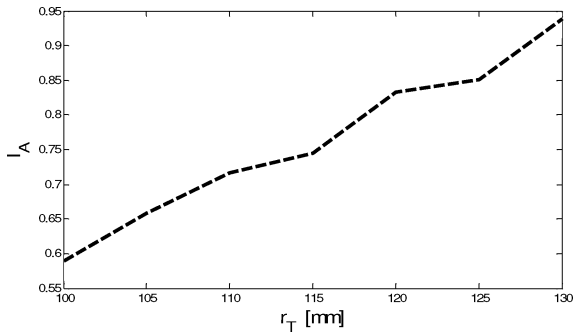

Fig. 19. Anthropomorphic arm I_A index.

Figure 17 shows the surface S_S (defined in Section 8.2). The link length has been derived from the values at which the effects of the robot stiffness are minimized (i.e., at which $I_{A,S}$ meets the maximum; Fig. 16).

As can be observed from Fig. 16 these link values allow 94% of the desired target surface to be reached by the manipulator.

Therefore Fig. 17 becomes the goal surface the designer has to achieve by modifying the mechanical properties of the robot, which influence the lumped parameters of the stiffness matrix.

Figure 18 shows the same surface under the effects of the robot accuracy. It can be observed that the reachability drops under 51% of the desired target surface, and the robot workspace becomes similar to that of NeuroMate for the considered surgical task.

Figure 19 shows the performance index I_A as a function of the radius of the TS. As for the NeuroMate manipulator the index decreases with the TS radius; then the deepest points on the cerebral tissue are unreachable.

Table IV. Values of the displacements limits.

Compliant displacements	Limits
$\sqrt{\Delta S_x^2 + \Delta S_y^2 + \Delta S_z^2}$	$\leq$0.01 mm
$\lvert\Delta S_\varphi\rvert, \lvert\Delta S_\psi\rvert, \lvert\Delta S_\theta\rvert$	$\leq 0.1^\circ$

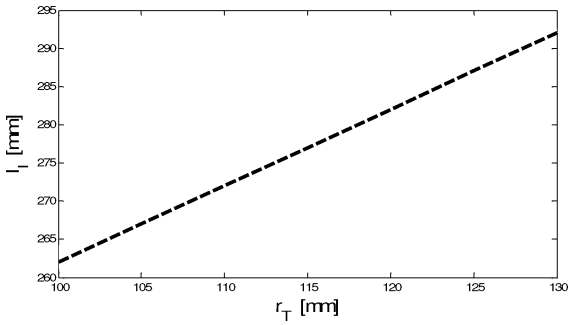

Fig. 20. Anthropomorphic arm I_I index.

The volume index for the considered lengths is $I_V = 0.91$. Therefore only one quarter of the considered target volume (Table IV) cannot be reached by the robot.

The invasiveness index I_I is shown in Fig. 20. Its value varies linearly with the TS radius. It must be recalled that the index is evaluated for all the reachable configurations without considerations of stiffness effects.

https://doi.org/10.1017/S026357470999035X Published online by Cambridge University Press

Table V. Stanford arm Denavit–Hartenber parameters.

i	${}^{i-1}T_i$	σ_i	a_i (mm)	α_i (rad)	d_i (mm)	θ_i (rad)
0	${}^{base}P_0$	1	0	0	530	0
1	${}^{0}P_1$	0	0	$-\frac{\pi}{2}$	412	q_1
2	${}^{1}P_2$	0	0	$\frac{\pi}{2}$	154	q_2
3	${}^{2}P_3$	1	0	0	q_3	0
4	${}^{3}P_4$	0	0	$-\frac{\pi}{2}$	0	q_4
5	${}^{4}P_5$	0	0	$\frac{\pi}{2}$	0	q_5
6	${}^{5}P_6$	0	0	0	263	q_6
	${}^{6}P_{\text{tool tip}}$	1	−85	0	138	0

The optimal cost function for the anthropomorphic manipulator is $p = 1.88$.

From the above analysis the anthropomorphic arm seems to allow better workspace performances in comparison to NeuroMate, but it requires much care to choose the suitable robot stiffness. The invasiveness index is up to 260 mm and is comparable to that of NeuroMate, if it refers to a wider workspace.

8.3.2. Stanford manipulator. The second robotic arm under analysis is the Stanford manipulator (Fig. 21), whose Denavit–Hartenberg parameters are shown in Table V and whose IKP can be solved by following the algorithm discussed in ref. [31].

The optimization problem works on d_2 and q_{3max}, since the robot workspace depends mainly on these values. As for the anthropomorphic arm, no constraints have been taken on the joint mobility. The elements of the diagonal matrix $\mathbf{K}_P$ are assumed be equal to $k_{T1} = k_{T2} = 4.67 \times 10^8$ Nm, $k_{T3} = 4.67 \times 10^{20}$ Nm, and $k_{T4} = k_{T5} = k_{T6} = 4.67 \times 10^6$ Nm in accordance with ref. [20].

Figure 22 shows the workspace index I_A versus the link lengths. It can be shown that the index I_A remains always much under the unit, so the robot does not allow reaching every point in the TS.

Figure 23 shows the surface S_S for the Stanford arm. As has been done for the anthropomorphic arm, the link length has been obtained from the links values at which the function $I_{A,S}$ achieves the maximum (Fig. 22). When the accuracy constraints are taken into consideration, the reachable surface must be reduced as in Fig. 24.

Figure 25 shows the performance index I_A as function of the radius of the TSs. The corresponding volume index for the Stanford arm is $I_V = 0.11$.

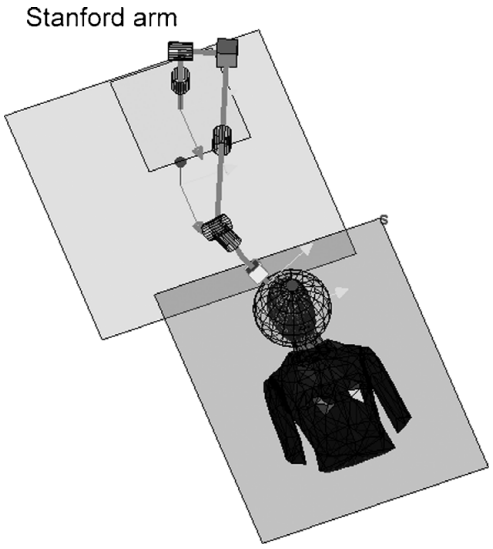

Fig. 21. Stanford arm.

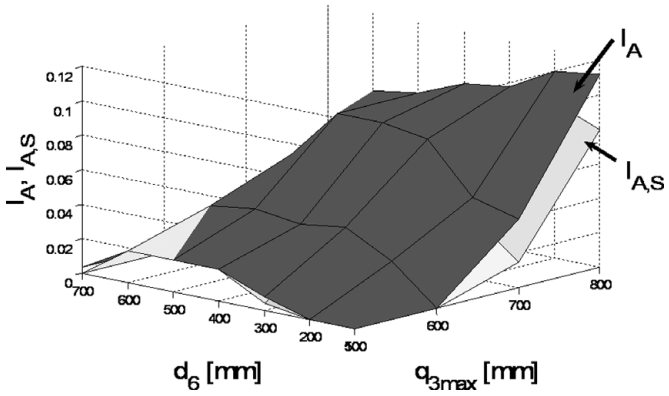

Fig. 22. Functions of I_A and $I_{A,S}$.

The invasiveness index I_I is shown in Fig. 26. Its value varies linearly with the TS radius as for NeuroMate and the anthropomorphic arm.

The cost object for the Stanford manipulator is $p = 0.24$.

By analyzing the index for Stanford arm it appears that this kinematic structure is not suitable for the considered neurosurgical task.

8.3.3. Neurobud manipulator. Neurobud is a special robot for neurosurgery whose particular structure has been conceived at the University of Udine. The robot kinematic is shown in Fig. 27, and its Denavit–Hartenberg parameters are described

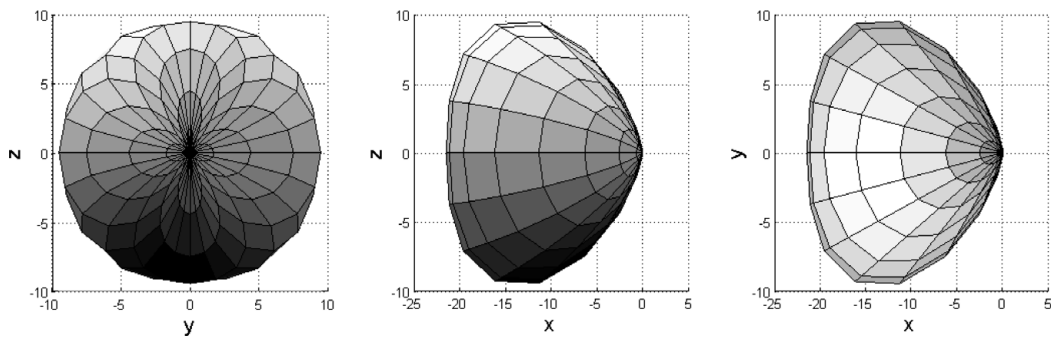

Fig. 23. Stanford arm S_S surface.

https://doi.org/10.1017/S026357470999035X Published online by Cambridge University Press

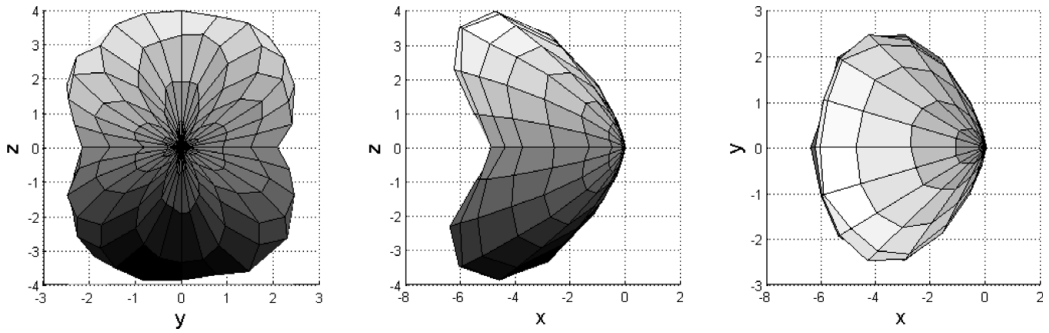

Fig. 24. Stanford arm S_S surface filtered by the accuracy constraints.

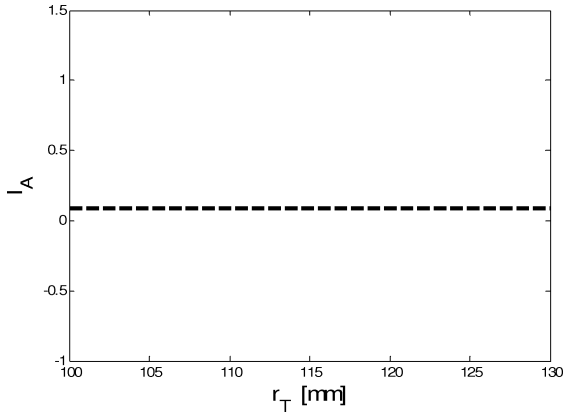

Fig. 25. Stanford arm I_A index.

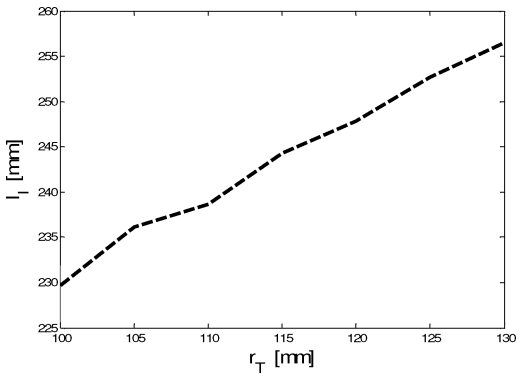

Fig. 26. Stanford arm I_I index.

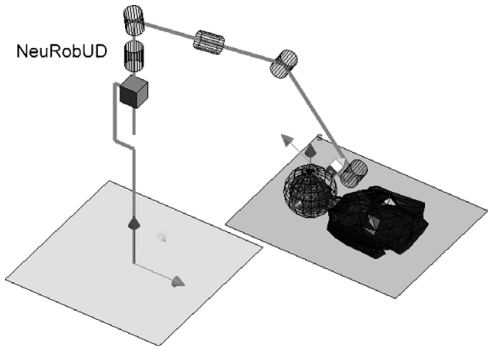

Fig. 27. Neurobud manipulator.

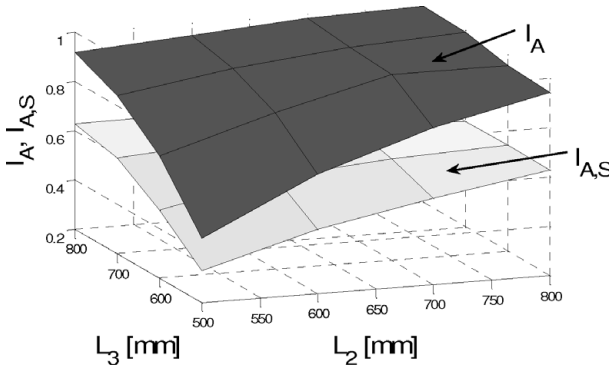

Fig. 28. Representation of I_A and $I_{A,S}$.

on Table VI. The complete analysis of Neurobud as well as the IKP solution can be found in ref. [30]. Owing to the particular kinematic structure, the optimization problem can search the optimal solution varying only the lengths of the second and third links. The elements of the diagonal matrix $\mathbf{K}_P$ have been assumed equal to $k_{T1} = 4.67 \times 10^{20}$ N m, $k_{T2} = k_{T3} = 4.67 \times 10^8$ N m, and $k_{T4} = k_{T5} = k_{T6} = 4.67 \times 10^6$ Nm according to those that have been used for the anthropomorphic arm.

Table VI. Neurobud Denavit–Hartenber parameters.

i	${}^{i-1}T_i$	σ_i	a_i (mm)	α_i (rad)	d_i (mm)	θ_i (rad)
1	${}^0P_1$	1	0	0	q_1	0
2	${}^1P_2$	0	0	$\frac{\pi}{2}$	450	q_2
3	${}^2P_3$	0	0	$-\frac{\pi}{2}$	0	q_3
4	${}^3P_4$	0	0	$\frac{\pi}{2}$	L2	q_4
5	${}^4P_5$	0	L3	0	0	q_5
6	${}^5P_6$	0	85	$\frac{\pi}{2}$	0	q_6
	${}^6P_{\text{tool tip}}$	1	0	0	138	0

Figure 28 shows the workspace index I_A versus the length of the chosen links. The complete reachability ($I_A = 1$) is achieved for $L_2 = L_3 = 800$ mm as for the anthropomorphic arm. From the function $I_{A,S}$ in Fig. 28 it can be observed that if the accuracy constraints are taken into account, the reachability drops as for the anthropomorphic arm. The maximum, $I_{A,S} = 0.65$, is achieved for $L_2 = 500$ and $d_4 = 800$. Figure 29 shows the surface S_S (defined in Section 8.3.1). The link length has been obtained, as in the previous case, from the values at which the function $I_{A,S}$ achieves the maximum (Fig. 28). Figure 30 shows the stiffness effects which reduce the extension of the surface S_S.

https://doi.org/10.1017/S026357470999035X Published online by Cambridge University Press

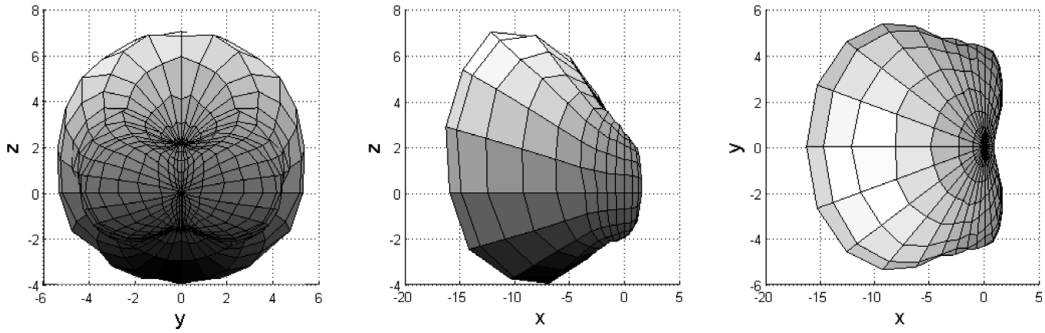

Fig. 29. Neurobud arm S_S surface.

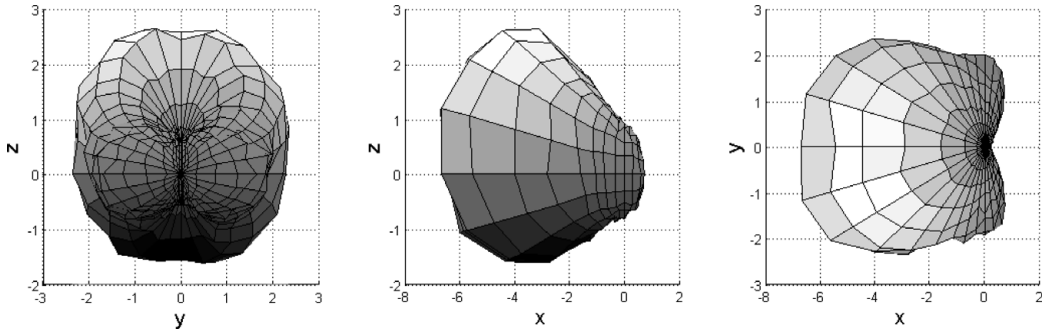

Fig. 30. Neurobud arm S_S surface filtered by the accuracy constraints.

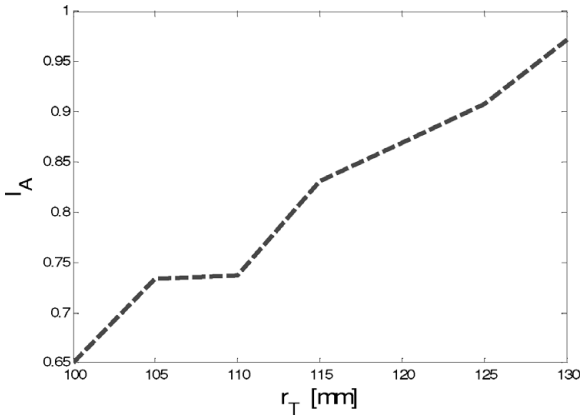

Fig. 31. For the Neurobud arm, $I_A(r_T)$.

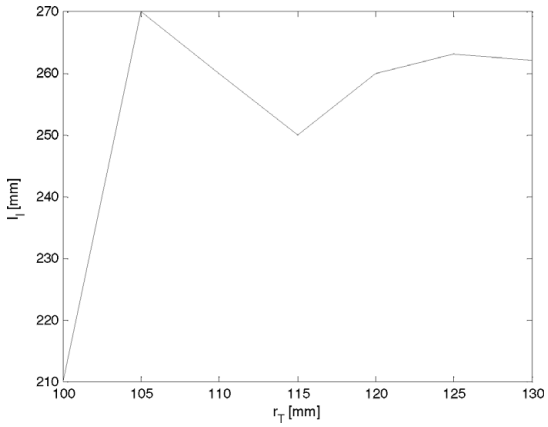

Fig. 32. For the Neurobud arm, $I_I(r_T)$.

The dependency of the performance index I_A on the radius of the TSs is shown in Fig. 31. The corresponding volume index is $I_V = 0.97$.

The invasiveness index I_I is shown in Fig. 32. It can be noted that different from what occurs for the previous robots, the invasiveness index stays near the same value into the considered range for the TS radius. Therefore the invasiveness is almost constant even if the radius increases.

The cost object for the Neurobud is $p = 1.97$.

From the analysis of the indices it appears that the Neurobud performances are similar to those of the anthropomorphic robot. Nevertheless as far as the stiffness effects are considered, the Neurobud allows a better accuracy in tool positioning.

Moreover the invasiveness index does not depend linearly on the TS radius, allowing a nearly constant value of invasiveness.

9. Conclusion

A large number of new surgical devices have been developed in the past decades in order to improve the operation outcomes. The dexterity and accuracy required by such devices are often unreachable if the surgeons are not assisted by a suitable system. This requirement explains the recent progress of the medical robotics. Therefore, several research groups focus their attention on the development of new surgical manipulators. Nevertheless, in the literature a design procedure for medical robotics is still missing. The novel contribution of this work consists in defining some performance indices which can be used to design new medical robots. In particular, this paper focused on the design of neurosurgical manipulators, since the neurosurgical requirements are more and more restrictive with respect the other surgical fields.

https://doi.org/10.1017/S026357470999035X Published online by Cambridge University Press

The proposed indices can be used in a multiobjective optimization problem, which helps the designer to choose the suitable robot configuration.

The feasibility of such indices has been demonstrated first in analyzing the performances of the commercial neurosurgical robot named NeuroMate. Then, through a suitable optimization problem, the indices have been used to choose the optimal robot kinematic structure for the given neurosurgical task. Once the suitable kinematic structure has been found for the particular surgical task, it is possible to reuse the performance indices defined above to further optimize the robot link lengths according to the constraints on the joint movements imposed by the physical properties of the joints.

Appendix: Inverse kinematics solution for NeuroMate

Let ${}^0\mathbf{T}_4$ describe the desired configuration (position and orientation) of a four-joint robot end-effector:

$${}^0\mathbf{T}_4 = \begin{bmatrix} s_x & n_x & a_x & p_x \\ s_y & n_y & a_y & p_y \\ s_z & n_z & a_z & p_z \\ 0 & 0 & 0 & 1 \end{bmatrix}.$$

In general, the inverse kinematics problem of a four-joint robot, as presented in [Manseur], consists of solving the following matrix equation:

$${}^0\mathbf{T}_4 = {}^0\mathbf{A}_1\,{}^1\mathbf{A}_2\,{}^2\mathbf{A}_3\,{}^3\mathbf{A}_4.$$

Now, we derive a four-joint reduced set of equation with a choice of end-effector frame in which $a_4 = d_4 = 0$ e $\alpha_4 = 0$ without any loss of generality. Recall that the equations expressing the quantities t_z, p_z, $\mathbf{p}\cdot\mathbf{a}$, and $\mathbf{p}\cdot\mathbf{p}$ are independent of the first and last joint variables when those joints are revolute.

The a_z Equation

The pose vector ${}^0\mathbf{a}_4$ is a unit vector given by

$${}^0\mathbf{a}_4 = {}^0\mathbf{R}_4\mathbf{z} = {}^0\mathbf{R}_1\,{}^1\mathbf{R}_2\,{}^2\mathbf{R}_3\,{}^3\mathbf{R}_4\mathbf{z} = {}^0\mathbf{R}_1\,{}^1\mathbf{R}_2\,{}^2\mathbf{R}_3\mathbf{z}, \quad \text{(A1)}$$

where the fact that $\alpha_4 = 0$ leads to

$${}^3\mathbf{R}_4\mathbf{z} = \begin{pmatrix} sin(\alpha_4)s_4 \\ -sin(\alpha_4)c_4 \\ cos(\alpha_4) \end{pmatrix} = \begin{pmatrix} 0 \\ 0 \\ 1 \end{pmatrix} = \mathbf{z}$$

has been recognized.

Since $a_z = {}^0\mathbf{a}_4 \cdot \mathbf{z}$,

$$a_z = {}^0\mathbf{a}_4 \cdot \mathbf{z} = {}^0\mathbf{R}_1\,{}^1\mathbf{R}_2\,{}^2\mathbf{R}_3\mathbf{z} \cdot \mathbf{z}. \quad \text{(A2)}$$

Equation (A2) can be modified by matrix manipulations as follows:

$${}^0\mathbf{R}_1^{-1}\,{}^0\mathbf{a}_4 = {}^1\mathbf{R}_2\,{}^2\mathbf{R}_3\mathbf{z} \cdot \mathbf{z},\ {}^0\mathbf{R}_1^{-1}\,{}^0\mathbf{a}_4 \cdot \mathbf{z} = {}^1\mathbf{R}_2\,{}^2\mathbf{R}_3\mathbf{z} \cdot \mathbf{z},$$
$${}^0\mathbf{a}_4 \cdot {}^0\mathbf{R}_1\mathbf{z} = {}^2\mathbf{R}_3\mathbf{z} \cdot {}^1\mathbf{R}_2^{-1}\mathbf{z}$$

or

$${}^0\mathbf{a}_4 \cdot {}^0\mathbf{R}_1\mathbf{z} - {}^2\mathbf{R}_3\mathbf{z} \cdot {}^1\mathbf{R}_2^{-1}\mathbf{z} = 0. \quad \text{(A3)}$$

Equation (A3) involves only joint variables 1 and 3, since

$${}^1\mathbf{R}_2^{-1}\mathbf{z} = \begin{pmatrix} 0 \\ \sin(\alpha_2) \\ \cos(\alpha_2) \end{pmatrix}$$

is a constant vector.

The p_z Equation

The position vector of the end-effector for a four-joint robot is given by

$${}^0\mathbf{p}_4 = {}^0\mathbf{R}_1\left({}^1\mathbf{R}_2\left({}^2\mathbf{R}_3\,{}^3\mathbf{p}_4 + {}^2\mathbf{p}_3\right) + {}^1\mathbf{p}_2\right) + {}^0\mathbf{p}_1 \quad \text{(A4)}$$

which reduces to

$${}^0\mathbf{p}_4 = {}^0\mathbf{R}_1\left({}^1\mathbf{R}_2\,{}^2\mathbf{p}_3 + {}^1\mathbf{p}_2\right) + {}^0\mathbf{p}_1 \quad \text{(A5)}$$

with a choice of F_4 that leads to $a_4 = d_4 = 0$, since that makes ${}^3\mathbf{p}_4 = 0$. Equation (A5) can be manipulated as:

$${}^0\mathbf{R}_1\left({}^1\mathbf{R}_2\,{}^2\mathbf{p}_3 + {}^1\mathbf{p}_2\right)$$
$$= {}^0\mathbf{p}_4 - {}^0\mathbf{p}_1\left({}^1\mathbf{R}_2\,{}^2\mathbf{p}_3 + {}^1\mathbf{p}_2\right) = {}^0\mathbf{R}_1^{-1}\left({}^0\mathbf{p}_4 - {}^0\mathbf{p}_1\right) \quad \text{(A6)}$$

Taking the inner product with $\mathbf{z}$ yields

$${}^1\mathbf{R}_2\,{}^2\mathbf{p}_3 \cdot \mathbf{z} + {}^1\mathbf{R}_2\,{}^1\mathbf{p}_2 \cdot \mathbf{z} = {}^0\mathbf{R}_1^{-1}\,{}^0\mathbf{p}_4 \cdot \mathbf{z} - {}^0\mathbf{R}_1^{-1}\,{}^0\mathbf{p}_1 \cdot \mathbf{z}. \quad \text{(A7)}$$

Since rotations leave inner products invariant, the following equalities can be used:

$${}^1\mathbf{R}_2\,{}^2\mathbf{p}_3 \cdot \mathbf{z} = {}^2\mathbf{p}_3 \cdot {}^1\mathbf{R}_2^{-1}\mathbf{z}$$

and

$${}^0\mathbf{R}_1^{-1}\,{}^0\mathbf{p}_4 \cdot \mathbf{z} = {}^0\mathbf{p}_4 \cdot {}^0\mathbf{R}_1\mathbf{z}$$

in Eq. (A7) to provide

$${}^0\mathbf{R}_1\mathbf{z} \cdot {}^0\mathbf{p}_4 - {}^1\mathbf{R}_2^{-1}\mathbf{z} \cdot {}^2\mathbf{p}_3 = {}^0\mathbf{R}_1^{-1}\,{}^0\mathbf{p}_1 \cdot \mathbf{z} + {}^1\mathbf{p}_2 \cdot \mathbf{z}. \quad \text{(A8)}$$

The left-hand side of Eq. (A7) is a function of only the first and third joint variables, while the right-hand side is

$${}^0\mathbf{R}_1^{-1}\,{}^0\mathbf{p}_1 \cdot \mathbf{z} + {}^1\mathbf{p}_2 \cdot \mathbf{z} = \begin{bmatrix} c_1 & -\cos(\alpha_1)s_1 & \sin(\alpha_1)s_1 \\ s_1 & \cos(\alpha_1)c_1 & -\sin(\alpha_1)c_1 \\ 0 & \sin(\alpha_1) & \cos(\alpha_1) \end{bmatrix}$$
$$\times \begin{pmatrix} a_1c_1 \\ a_1s_1 \\ d_1 \end{pmatrix} \cdot \begin{pmatrix} 0 \\ 0 \\ 1 \end{pmatrix} + \begin{pmatrix} a_2c_2 \\ a_2s_2 \\ d_2 \end{pmatrix} \cdot \begin{pmatrix} 0 \\ 0 \\ 1 \end{pmatrix} = d_1\cos(\alpha_1) + d_2$$

and is independent of any revolute joint variable.

The a·p equation

The next equation is derived from the inner product ${}^0\mathbf{a}_4 \cdot \mathbf{p}$. Left-multiplying both sides of Eq. (A6) by ${}^1\mathbf{R}_2^{-1}$ gives

$${}^2\mathbf{p}_3 + {}^1\mathbf{R}_2^{-1}\,{}^1\mathbf{p}_2 = {}^1\mathbf{R}_2^{-1}\,{}^0\mathbf{R}_1^{-1}\left({}^0\mathbf{p}_4 - {}^0\mathbf{p}_1\right). \quad \text{(A9)}$$

https://doi.org/10.1017/S026357470999035X Published online by Cambridge University Press

Equation (A1) gives an expression for end-effector frame unit vector ${}^0\mathbf{a}_4$ and can be modified into

$$ {}^1\mathbf{R}_2^{-1}\,{}^0\mathbf{R}_1^{-1}\,{}^0\mathbf{a}_4 = {}^2\mathbf{R}_3\mathbf{z} \tag{A10} $$

by left-multiplication with ${}^1\mathbf{R}_2^{-1}\,{}^0\mathbf{R}_1^{-1}$. The inner product of opposite sides of Eqs. (A9) and (A10) provides

$$ \left({}^2\mathbf{p}_3 + {}^1\mathbf{R}_2^{-1}\,{}^1\mathbf{p}_2\right)\cdot {}^2\mathbf{R}_3\mathbf{z} = {}^1\mathbf{R}_2^{-1}\,{}^0\mathbf{R}_1^{-1} \times \left({}^0\mathbf{p}_4 - {}^0\mathbf{p}_1\right)\cdot {}^1\mathbf{R}_2^{-1}\,{}^0\mathbf{R}_1^{-1}\,{}^0\mathbf{a}_4 $$

which simplifies to

$$ {}^2\mathbf{p}_3\cdot {}^2\mathbf{R}_3\mathbf{z} + {}^1\mathbf{R}_2^{-1}\,{}^1\mathbf{p}_2\cdot {}^2\mathbf{R}_3\mathbf{z} = {}^0\mathbf{p}_4\cdot {}^0\mathbf{a}_4 - {}^0\mathbf{p}_1\cdot {}^0\mathbf{a}_4 $$

or

$$ {}^0\mathbf{p}_1\cdot {}^0\mathbf{a}_4 + {}^1\mathbf{R}_2^{-1}\,{}^1\mathbf{p}_2\cdot {}^2\mathbf{R}_3\mathbf{z} = {}^0\mathbf{p}_4\cdot {}^0\mathbf{a}_4 - {}^2\mathbf{R}_3^{-1}\,{}^2\mathbf{p}_3\cdot\mathbf{z}. \tag{A11} $$

Equation (A11) is also independent of joint variables 2 and 4.

The p·p equation

From Eq. (A5), the length squared of the end-effector position vector $\mathbf{p}$ is

$$ {}^0\mathbf{p}_4\cdot {}^0\mathbf{p}_4 = \left[{}^0\mathbf{R}_1\left({}^1\mathbf{R}_2\,{}^2\mathbf{p}_3 + {}^1\mathbf{p}_2\right) + {}^0\mathbf{p}_1\right]\cdot\left[{}^0\mathbf{R}_1\left({}^1\mathbf{R}_2\,{}^2\mathbf{p}_3 + {}^1\mathbf{p}_2\right) + {}^0\mathbf{p}_1\right]. \tag{A12} $$

By use of inner-product invariance under rotation, Eq. (A12) can be expressed as

$$ {}^2\mathbf{p}_3\cdot {}^1\mathbf{R}_2^{-1}\,{}^1\mathbf{p}_2 + {}^0\mathbf{p}_4\cdot {}^0\mathbf{p}_1 = \frac{\left[{}^0\mathbf{p}_4\cdot {}^0\mathbf{p}_4 + {}^0\mathbf{p}_1\cdot {}^0\mathbf{p}_1 - {}^1\mathbf{p}_2\cdot {}^1\mathbf{p}_2 - {}^2\mathbf{p}_3\cdot {}^2\mathbf{p}_3\right]}{2}. \tag{A13} $$

The right side of Eq. (A13) is constant, and the left side depends only on joint variables 1 and 3.

Equations (A3), (A8), (A11), and (A13) form a linear system of four equation in sines and cosines of θ_1 e θ_3. Indeed, the equations provide

$$ \sin(q_4)\sin(\alpha_4)a_3 + a_2(\cos(q_2)a_x + \sin(q_2)a_y) - \cos(q_4)\sin(\alpha_3)\sin(\alpha_4)d_3 = e_1, \tag{A14} $$

$$ \cos(q_4)\sin(\alpha_3)\sin(\alpha_4) + \sin(q_2)\sin(\alpha_2)a_x - \cos(q_2)\sin(\alpha_2)a_y = e_2, \tag{A15} $$

$$ \sin(\alpha_2)(\sin(q_2)p_x - \cos(q_2)p_y) - \sin(q_4)\sin(\alpha_3)a_4 = e_3, \tag{A16} $$

$$ \cos(q_4)a_3a_4 + \sin(q_4)\sin(\alpha_3)d_3a_4 + a_2(\cos(q_2)p_x + \sin(q_2)p_y) = e_4, \tag{A17} $$

with the right-side constants given by

$$ \begin{aligned} e_1 &= -\cos(\alpha_3)\cos(\alpha_4)d_3 - \cos(\alpha_4)d_4 + a_xp_x + a_yp_y + a_z(p_z - d_2),\\ e_2 &= \cos(\alpha_3)\cos(\alpha_4) - \cos(\alpha_2)a_z,\\ e_3 &= \cos(\alpha_2)(d_2 - a_z) + d_3 + \cos(\alpha_3)d_4,\\ e_4 &= \frac{1}{2}\left(a_2^2 - a_3^2 - a_4^2 + d_2^2 - d_3^2 - d_4^2 + p_x^2 + p_y^2 + p_z^2 - 2\cos(\alpha_3)d_3d_4 - 2d_2p_z\right). \end{aligned} $$

The linear system of Eqs. (A14) – (A17) can be expressed in matrix form using

$$ \mathbf{H} = \begin{bmatrix} a_2a_y & a_2a_x & \sin(\alpha_4)a_3 & -\sin(\alpha_3)\sin(\alpha_4)d_3\\ \sin(\alpha_2)a_x & -\sin(\alpha_2)a_y & 0 & \sin(\alpha_3)\sin(\alpha_4)\\ \sin(\alpha_2)p_x & -\sin(\alpha_2)p_y & -\sin(\alpha_3)a_4 & 0\\ a_2p_y & a_2p_x & \sin(\alpha_3)a_4d_3 & a_3a_4 \end{bmatrix} $$

as

$$ \mathbf{H}\cdot\begin{pmatrix} s_1\\ c_1\\ s_3\\ c_3 \end{pmatrix} = \begin{pmatrix} e_1\\ e_2\\ e_3\\ e_4 \end{pmatrix}. $$

Now we consider ${}^0\mathbf{P}_5$ as the matrix that describes the desired configuration (position and orientation) of the NeuroMate end-effector,

$$ {}^0\mathbf{P}_5 = \begin{bmatrix} s_x & n_x & a_x & p_x\\ s_y & n_y & a_y & p_y\\ s_z & n_z & a_z & p_z\\ 0 & 0 & 0 & 1 \end{bmatrix}, $$

which can be manipulated into

$$ {}^1\mathbf{Q}_5 = \begin{bmatrix} m_x & c_x & u_x & q_x\\ m_y & c_y & u_y & q_y\\ m_z & c_z & u_z & q_z\\ 0 & 0 & 0 & 1 \end{bmatrix} = {}^0\mathbf{A}_1^{-1}\,{}^0\mathbf{P}_5 = {}^1\mathbf{A}_2\,{}^2\mathbf{A}_3\,{}^3\mathbf{A}_4\,{}^4\mathbf{A}_5 $$

$$ = \begin{bmatrix} \cos(q_1)s_x + \sin(q_1)s_y & \cos(q_1)n_x + \sin(q_1)n_y & \cos(q_1)a_x + \sin(q_1)a_y & \cos(q_1)p_x + \sin(q_1)p_y - 125\\ \cos(q_1)s_y - \sin(q_1)s_x & \cos(q_1)n_y - \sin(q_1)n_x & \cos(q_1)a_y - \sin(q_1)a_x & \cos(q_1)p_y - \sin(q_1)p_x\\ s_z & n_z & a_z & p_z\\ 0 & 0 & 0 & 1 \end{bmatrix}. \tag{A18} $$

https://doi.org/10.1017/S026357470999035X Published online by Cambridge University Press

Considering now ${}^1\mathbf{Q}_5$, instead of ${}^0\mathbf{T}_4$, Eq. (A18) can be rewriten as

$$\mathbf{H}\cdot\begin{pmatrix}s_2\\c_2\\s_4\\c_4\end{pmatrix}=\begin{pmatrix}e_1\\e_2\\e_3\\e_4\end{pmatrix} \tag{A19}$$

with the new matrix $\mathbf{H}$, equal to

$$\mathbf{H}=\begin{bmatrix} a_2u_y & a_2u_x & \sin(\alpha_4)a_3 & -\sin(\alpha_3)\sin(\alpha_4)d_3\\ \sin(\alpha_2)u_x & -\sin(\alpha_2)u_y & 0 & \sin(\alpha_3)\sin(\alpha_4)\\ \sin(\alpha_2)q_x & -\sin(\alpha_2)q_y & -\sin(\alpha_3)a_4 & 0\\ a_2q_y & a_2q_x & \sin(\alpha_3)a_4d_3 & a_3a_4\end{bmatrix},$$

and vector $\mathbf{e}$,

$$\mathbf{e}=\begin{pmatrix}e_1\\e_2\\e_3\\e_4\end{pmatrix}=\begin{pmatrix}-\cos(\alpha_3)\cos(\alpha_4)d_3-\cos(\alpha_4)d_4+u_xq_x+u_yq_y+u_z(q_z-d_2)\\ \cos(\alpha_3)\cos(\alpha_4)-\cos(\alpha_2)u_z\\ \cos(\alpha_2)(d_2-u_z)+d_3+\cos(\alpha_3)d_4\\ \frac{1}{2}(\mathbf{q}\cdot\mathbf{q}+a_2^2-a_3^2-a_4^2+d_2^2-d_3^2-d_4^2-2\cos(\alpha_3)d_3d_4-2d_2p_z)\end{pmatrix}.$$

and vector $\mathbf{e}$ results in

$$\begin{pmatrix}e_1\\e_2\\e_3\\e_4\end{pmatrix}=\begin{bmatrix}a_x(p_x-125\cos(q_1))+a_y(p_y-125\sin(q_1))+a_z(p_z-148)\\ 1\\ 0\\ \frac{1}{2}\left(p_x^2-250\cos(q_1)p_x+p_y^2+p_z^2-250\sin(q_1)p_y-296p_z-207471\right)\end{bmatrix}.$$

The matrix Eq. (A19) calculated for robot NeuroMate gives the following four equations:

$$0=(p_x-125\cos(q_1))a_x+(p_y-125\sin(q_1))a_y+(p_z-148)a_z, \tag{A20}$$

$$\cos(q_1+q_2)a_y-\sin(q_1+q_2)a_x=1, \tag{A21}$$

$$125\sin(q_2)-\sin(q_1+q_2)p_x+\cos(q_1+q_2)p_y=0, \tag{A22}$$

$$122500\cos(q_4)=\frac{1}{2}\left(p_x^2-250\cos(q_1)p_x+p_y^2+p_z^2-250\sin(q_1)p_y-296p_z-207471\right). \tag{A23}$$

The solutions for the joint variable q_1 are computed from Eq. (A20) and result in

$$q_{1,1}=-\arccos\left[\frac{1}{125\left(a_x^2+a_y^2\right)}(p_xa_x^2+p_ya_ya_x+p_za_za_x-148a_za_x+..\right.$$
$$\left.-\sqrt{-a_y^2\left(\left(p_x^2-15625\right)a_x^2+2p_x\left(p_ya_y+(p_z-148)a_z\right)a_x+\left(p_y^2-15625\right)a_y^2+(p_z-148)^2a_z^2+2p_y(p_z-148)a_ya_z\right)}\right],$$

$$q_{1,3}=-\arccos\left[\frac{1}{125\left(a_x^2+a_y^2\right)}(p_xa_x^2+p_ya_ya_x+p_za_za_x-148a_za_x+..\right.$$
$$\left.+\sqrt{-a_y^2\left(\left(p_x^2-15625\right)a_x^2+2p_x\left(p_ya_y+(p_z-148)a_z\right)a_x+\left(p_y^2-15625\right)a_y^2+(p_z-148)^2a_z^2+2p_y(p_z-148)a_ya_z\right)}\right],$$

$$q_{1,2}=-q_{1,2},\quad q_{1,4}=-q_{1,3}.$$

Substituting the expressions of u_x, u_y, q_x, and q_y and calculating the matrix $\mathbf{H}$ with the NeuroMate parameters results i

$$\mathbf{H}=\begin{bmatrix}0 & 0 & 0 & 0\\ -\cos(q_1)a_x-\sin(q_1)a_y & \cos(q_1)a_y-\sin(q_1)a_x & 0 & 0\\ -\cos(q_1)p_x-\sin(q_1)p_y+125 & \cos(q_1)p_y-\sin(q_1)p_x & 0 & 0\\ 0 & 0 & 0 & 122500\end{bmatrix}$$

The values of the two joint variables, q_2 and q_4, can be computed from Eqs. (A21) and (A22), as follows:

$$q_{2,1}=-\arccos\times\left(\frac{\cos(q_1)p_x+\sin(q_1)p_y-125}{(125\sin(q_1)-p_y)a_x+(p_x-125\cos(q_1))a_y}\right),$$
$$q_{2,2}=-q_{2,1}.$$

The values of the remaining joint variable q_3 can be computed expanding vector Eq. (A6) (referred to the matrix ${}^1\mathbf{Q}_5$, instead of ${}^0\mathbf{T}_4$) and obtaining the following two component equations

https://doi.org/10.1017/S026357470999035X Published online by Cambridge University Press

with the NeuroMate parameters:

$$\cos(q_3)(350\cos(q_4)+350)-350\sin(q_3)\sin(q_4) = \sin(q_2)(\cos(q_1)p_y-\sin(q_1)p_x) + \cos(q_2)(\cos(q_1)p_x+\sin(q_1)p_y-125) \quad \text{(A24)}$$

and

$$(350\cos(q_4)+350)\sin(q_3) + 350\cos(q_3)\sin(q_4) = 148-p_z. \quad \text{(A25)}$$

Equations (A24) and (A25) can be easily solved to provide the follows two solutions for q_3:

$$q_{3,1} = -\arccos\left(\frac{1}{700}\left(-125\cos(q_2)+\cos(q_1+q_2)p_x + \sin(q_1+q_2)p_y - p_z\tan\left(\frac{q_4}{2}\right)+148\tan\left(\frac{q_4}{2}\right)\right)\right),$$

$$q_{3,2} = \arccos\left(\frac{1}{700}\left(-125\cos(q_2)+\cos(q_1+q_2)p_x + \sin(q_1+q_2)p_y - p_z\tan\left(\frac{q_4}{2}\right)+148\tan\left(\frac{q_4}{2}\right)\right)\right).$$

The last joint variable, θ_5, can then be obtained by considering the first column vector ${}^0\mathbf{s}_5$ of the orientation matrix ${}^0\mathbf{R}_5$ as

$${}^4\mathbf{R}_5\mathbf{x} = \begin{pmatrix} c_5 \\ s_5 \\ 0 \end{pmatrix} = {}^3\mathbf{R}_4^{-1}\,{}^2\mathbf{R}_3^{-1}\,{}^1\mathbf{R}_2^{-1}\,{}^0\mathbf{R}_1^{-1}\,{}^0\mathbf{R}_4^{-1}\mathbf{x} = {}^3\mathbf{R}_4^{-1}\,{}^2\mathbf{R}_3^{-1}\,{}^1\mathbf{R}_2^{-1}\,{}^0\mathbf{R}_1^{-1}\begin{pmatrix} s_x \\ s_y \\ s_z \end{pmatrix},$$

where

$$\mathbf{x} = \begin{pmatrix} 1 \\ 0 \\ 0 \end{pmatrix},$$

and solving for

$$c_5 = \cos(q_1+q_2)\cos(q_3+q_4)s_x + \cos(q_3+q_4)\sin(q_1+q_2)s_y - \sin(q_3+q_4)s_z,$$

$$s_5 - co = s(q_1+q_2)\sin(q_3+q_4)s_x - \sin(q_1+q_2)\sin(q_3+q_4)s_y - \cos(q_3+q_4)s_z,$$

$$q_5 = a\tan 2(s_5, c_5).$$

Observing the solutions reported above, we can say that in general four different robot configurations exist, corresponding to the solution vectors $\mathbf{Q}_i = [q_1, q_2, q_3, q_4, q_5]$, $i = 1 \div 4$, of the IKP.

References

1. A. L. Benabid and W. L. Nowinski, "Intraoperative robotics for the practice of neurosurgery: a surgeon's perspective," **In**: *The Operating Room for the 21st Century* (M. L. Apuzzo, ed.) (AANS, 2003) pp. 103–118.
2. P. B. McBeth, D. F. Louw, P. R. Rizun and G. R. Sutherland, "Robotics in Neurosurgery," *Am. J. Surg.* **188**(4, Suppl. 1), 68–75 (Oct. 2004).
3. P. L. Gildenberg, "What is stereotactic surgery?" available at http://www.stereotactic:net=whatis.htm (Huston Stereotactic Center).
4. C. W. Burckhart, P. Flury and D. Glauser, "Stereotactic brain surgery," *IEEE Eng. Med. Biol.* **14**, 314–317 (1995).
5. Y. S. Kwoh, J. Hou, E. A. Jonckheere and S. Hayati, "A robot with improved absolute positioning accuracy for CT guided stereotactic brain surgery," *IEEE Trans. Biomed. Eng.* **35**(2), 153–160 (1988).
6. T. H. Wagner, Y. Taeil, S. L. Meeks, F. J. Bova, B. L. Brechner, C. Yunmei, J. M. Buatti, W. A. Friedman, K. D. Foote and L. G. Bouchet, "A geometrically based method for automated radiosurgery planning," *Int. J. Rad. Oncol. Biol. Phys*. **48**(5), 1599–1611 (Dec. 2000).
7. Y. S. Kwoh, J. Hou, E. A. Jonckheere and S. Hayati, "A robot with improved absolute positioning accuracy for CT guided stereotactic brain surgery," *IEEE Trans. Biomed. Eng.* **35**, 153–160 (1988).
8. J. M. Drake, M. Joy, A. Goldenberg and D. Kreindler, "Computer- and robot-assisted resection of thalamic astrocytomas in children," *Neurosurgery* **29**, 27–31 (1991).
9. A. L. Benabid, P. Cinquin, S. Lavalle, J. F. Le Bas, J. Demongeot and J. de Rougemont, "Computer-driven robot for stereotactic surgery connected to CT scan and magnetic resonance imaging: Technological design and preliminary results," *Appl. Neurophysiol.* **50**, 153–154 (1987).
10. P. B. McBeth, D. F. Louw, P. R. Rizun and G. R. Sutherland, "Robotics in neurosurgery" *Am. J. Surg.* **188**(4, Suppl. 1), 68–75 (Oct. 2004).
11. Q. Li, L. Zamorano, A. Pandya, R. Perez, J. Gong and F. Diaz, "The application accuracy of the NeuroMate robot – a quantitative comparison with frameless and frame-based surgical localization systems," *Comp. Aid. Surg.* **7**, 90–98 (2002).
12. K. Hongo, T. Goto, Y. Kakizawa, J.-I. Koyama, T. Kawai, K. Kan, Y. Tanaka and S. Kobayashi, "Micromanipulator system (NeuRobot): Clinical application in neurosurgery," *Int. Congr. Ser.* **1256**, 509–513 (Jun. 2003).
13. T. Miyahara, T. Goto, Y. Kakizawa, J. Koyama, Y. Tanaka and K. Hongo, "Neurosurgical telecontrolled micromanipulator system (NeuRobot): Clinically applied cases and further development," *Int. Congr. Ser.* **1281**, 1363 (May 2005).
14. M. D. Michael, R. Krishnanand A. Raabe, "Robot-assisted navigated neuroendoscopy," *Neurosurgery* **51**(6), 1446–1452 (Dec. 2002).
15. Z. Tian, J. Liu, Y. Zhang, T. Wang and H. Xing, "Neuromaster: a robot system for neurosurgery," *IEEE International Conference on Robotics and Automation, ICRA 2004*, New Orleans, LA (26 April to 1 May 2004), 821–828.
16. S. Kucuk and Z. Bingul, "Robot workspace optimization based on a novel local and global performance indices," *IEEE International Symposium on Industrial Electronics, ISIE 2005*, Dubrovnik, Croatia (20–23 June 2005) 1593–1598.
17. S. Kucuk and Z. Bingul, "Comparative study of performance indices for fundamental robot manipulators," *Rob. Auton. Syst.* **54**, 567–573 (2006).
18. R. V. Mayorg, J. Carrera and M. M. Oritz, "A kinematics performance index based on the rate of change of a standard isotropy condition for robot design optimization," *Rob. Auton. Syst.* **53**, 153–163 (2005).
19. G. Nawratil, "New performance indices for 6R robots," *Mech. Mach. Theory* **42**, 1499–1511 (2007).
20. G. Carbone, E. Ottaviano and M. Ceccarelli, "An optimum design procedure for both serial and parallel manipulators," *J. Mech. Eng. Sci.* **221**(7), 829–843 (2007).

https://doi.org/10.1017/S026357470999035X Published online by Cambridge University Press

21. C. Gosselin and J. Angeles, "The optimum kinematic design of a planar three-degree-of-freedom parallel manipulator," *ASME J. Mech. Transm. Autom. Des.* **110**, 35–41 (1988).
22. F. C. Park, "Optimal robot design and differential geometry," *Trans. ASME* **117**, 87–92 (1995).
23. M. Ceccarelli, "A synthesis algorithm for three-revolute manipulators by using an algebraic formulation of workspace boundary," *ASME J. Mech. Des.* **117**, 298–302 (1995).
24. G. Carbone and M. Ceccarelli, "A Serial-parallel robotic architecture for surgical tasks," *Robotica* **23**(3), 345–354 (May 2005). Doi: 10.1017/S0263574704000967.
25. E. I. Rivin, *Stiffness and Damping in Mechanical Design* (Marcel Dekker, New York, 1999).
26. H. Kardestuncer. *Elementary Matrix Analysis of Structures* (McGraw-Hill, Kogakusha, Tokyo, 1974).
27. G. R. Cosgrove, F. H. Hochberg and, N. T. Zervas, et al., "Interstitial irradiation of brain tumors, using a miniature radiosurgery device: initial experience," *Neurosurgery* **40**, 518–525 (1997).
28. A. Rossi, A. Trevisani and V. Zanotto, "A telerobotic haptic system for minimally invasive stereotactic neurosurgery," *Int. J. Med. Rob. Comp. Assisted Surg.*. **1**(2), 64–75 (2005).
29. A. Rossi, A. Gasparetto, A. Trevisani and V. Zanotto, "A robotic approach to stereotacticradio-surgery," *Proceedings of the 7th Biennial ASME Conference on Engineering Systems Design and Analysis*, Manchester, UK (Jul. 2004) pp. 19–22.
30. A. Gasparetto, R. Vidoni, V. Zanotto, "NEUROBUD: A novel robot for neurosurgery," *Proceedings of the the 16th International Workshop in Alpe-Adria Danube Region (RAAD 2007)*, Ljubljana, Slovenia (June 7–9, 2007).
31. L. Sciavicco and B. Siciliano, *Modelling and Control of Robot Manipulators*, Advanced Textbooks in Control and Signal Processing Series (Springer, London, UK, 2000).
32. Manseur Rachid, Robot Modeling and kinematics, Da Vinci Engineering Press (April 2006).

https://doi.org/10.1017/S026357470999035X Published online by Cambridge University Press